Supporting Information

Electron Microscopy Characterisation of P3 Lines and Laser Scribing-induced Perovskite Decomposition in Perovskite Solar Modules

Felix Utama Kosasih[†,*], Lucija Rakocevic[‡,§], Tom Aernouts[‡], Jef Poortmans[‡,§], Caterina Ducati[†,*]

[†]Department of Materials Science & Metallurgy, University of Cambridge, 27 Charles Babbage Road, Cambridge CB3 0FS, United Kingdom

[‡]imec, Thin Film PV Group, Photovoltaics Department, Kapeldreef 75, 3001 Leuven, Belgium

[§]Departement Electrotechniek – ESAT, KU Leuven, 3001 Leuven, Belgium

[*]fuk21@cam.ac.uk, cd251@cam.ac.uk

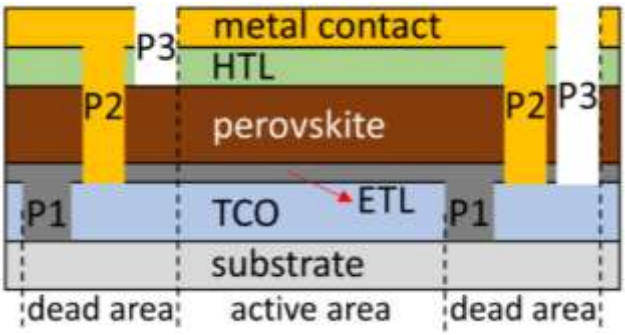

Figure S1. Schematic of an n-i-p perovskite solar cell with two sets of P1-P3 scribe lines, one with shallow P3 (left) and one with deep P3 (right). H(E)TL is hole (electron) transport layer and TCO is transparent conductive oxide.

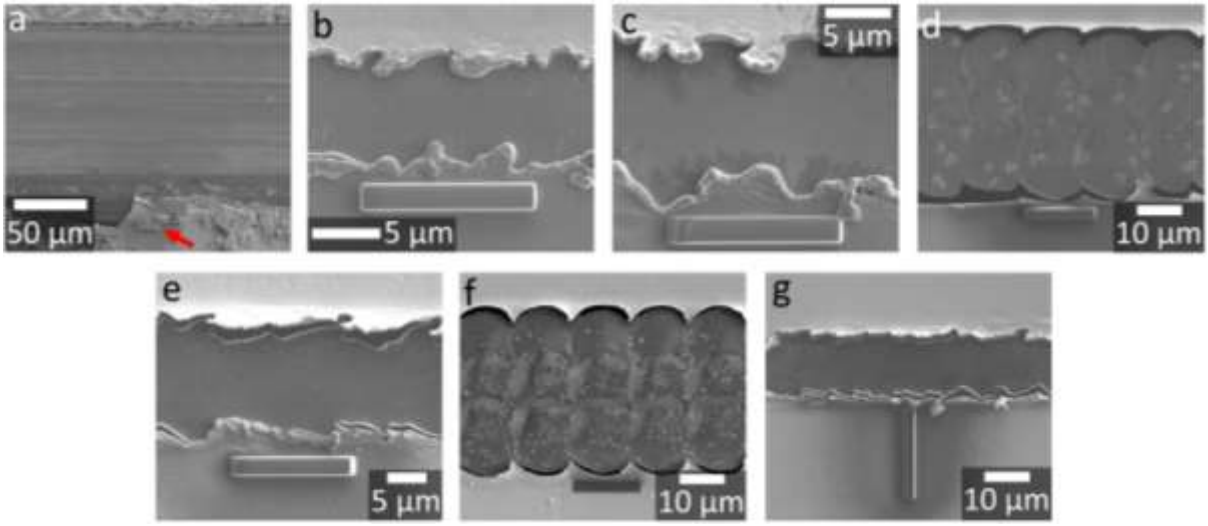

Figure S2. Location of the lamellae cut for STEM characterisation for samples (a) SC, (b) SD-3.47, (c) SD-3.04, (d) SS, (e) BD, (f) BS, and (g) SD-3.04. After cut from a cell, each lamella is thinned down from both sides to ~200 nm thickness. Therefore, the distance between the scribe line edge and final lamella is approximately 900 nm for those cut parallel to P3 line (a-f).

Supplementary Note 1

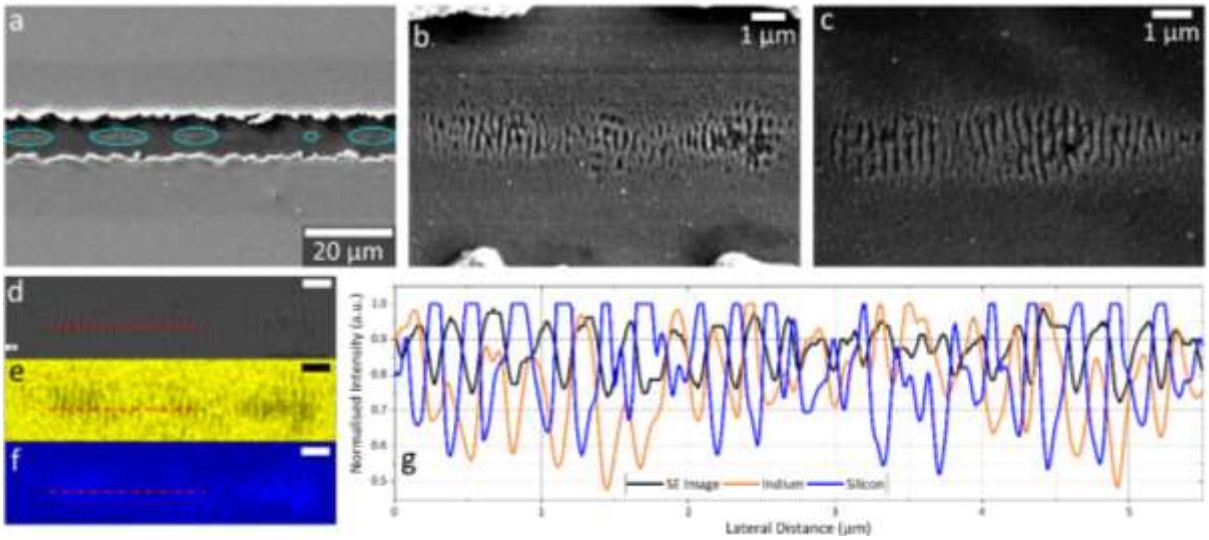

Figure S3. (a-c) Top-view SEM images of sample SD-3.47's damaged ITO layer. (d) EDX scan area for (e-f). (e) In and (f) Si maps showing low In and high Si signal at the scratches. (g) Normalised intensity line plots of the red dashed lines in (d-f) The dips in SE Image line indicate the damage marks' locations. Scale bars in (d-f) are 1 µm.

The periodic nature of damage marks shown in Figure S3 suggests that they are a form of laser-induced periodic surface structures (LIPSS). More specifically, the similarity between their periodicity (265 ± 46 nm) and the laser pulse's wavelength (355 nm) indicates that these damage marks are a low spatial frequency LIPSS – type 1 (LSFL-I) according to Bonse and co-workers' LIPSS classification.[1] Previous works have established that LSFL-I is caused by interference between the incident laser pulses and reflected or scattered waves at a rough surface.[1,2] These scattered waves can be either the laser pulse itself or, in the case of fs-pulse laser, surface plasmon polaritons (SPPs) generated in the material.[3–6] This requirement for an fs-pulse laser is important because it allows transient changes of the material's permittivity, allowing excitation of SPPs even in dielectrics and semiconductors. Therefore, SPPs are not involved in this study since a ps-pulse laser was used and thus the interference was only between the incident and scattered laser waves. Another theory suggests that even in cases where the laser energy that arrives at a rough surface is not enough for material ablation, it is still possible to form LSFL-I through rapid local melting and subsequent re-solidification as long as the interference requirement is satisfied.[7,8] Regardless of the active mechanism, laser fluence and pulse overlap have a large effect on LIPSS formation. Sufficiently high fluence is needed to excite SPPs and/or melt the material. Meanwhile, a high overlap ratio assists LIPSS formation because the rough material surface created by an earlier pulse amplifies wave scattering of subsequent pulses.[1] These two parameters explain why LIPSS was only observed in sample SD-3.47 in this work.

Supplementary Note 2

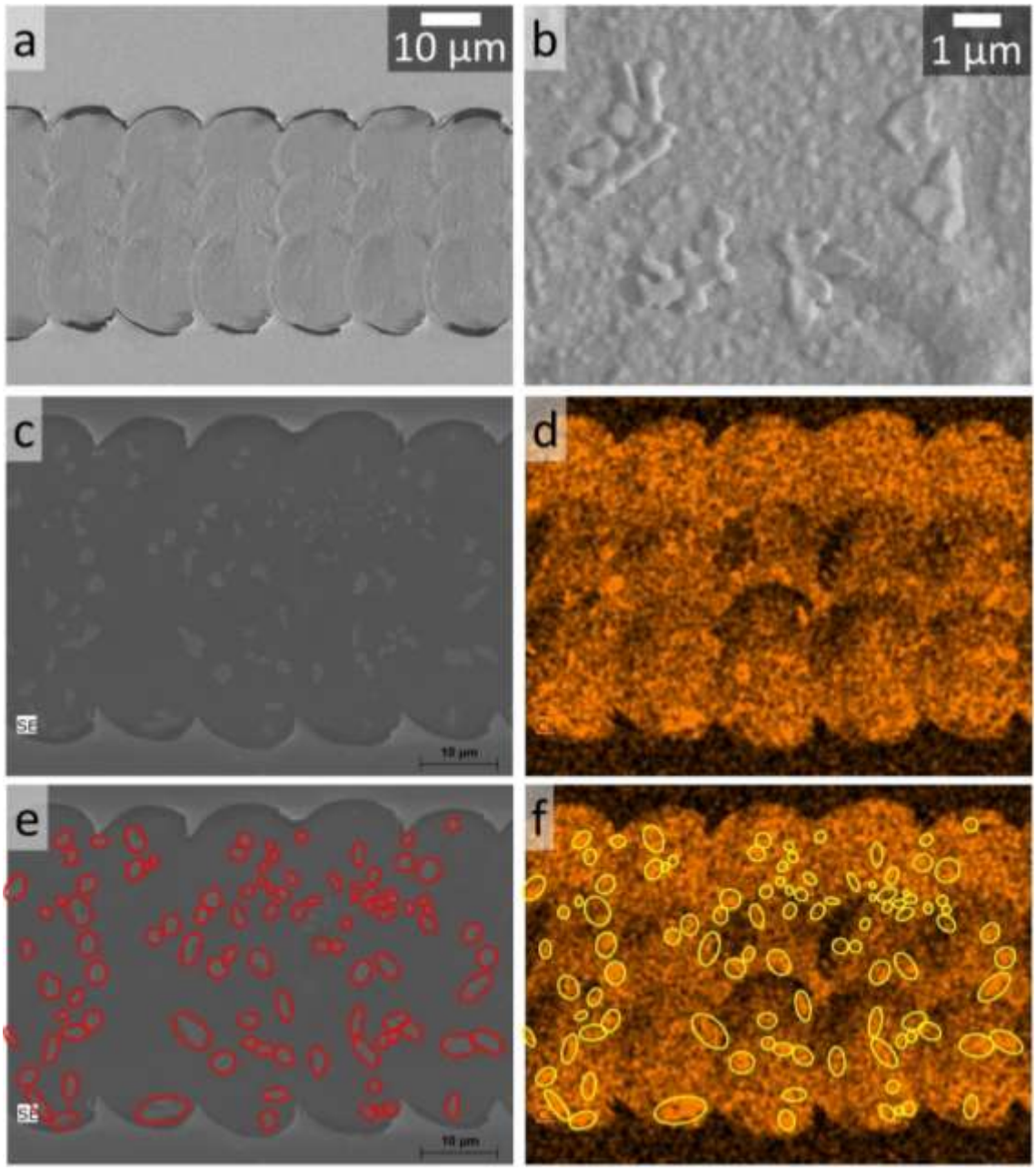

Figure S4. (a,b) Backscattered electron images of sample SS, acquired with 5 kV acceleration voltage. (c) Secondary electron image and (d) Cs map of a P3 line in sample SS. (e) and (f) are reproductions of (c) and (d) with red/yellow markers to highlight the correlation between grains and regions of high Cs intensity. Scale bars in (c) and (e) applies for (d) and (f) as well.

Secondary electron images are sensitive to the sample's topography (bright for tilted surfaces, dark for flat) while the contrast in backscattered electron images is dominated by high-Z elements.[9] Figure S4a,b show that the large grains on the scribe line's surface have the same heavy elements as the perovskite layer underneath them, namely Cs, Pb, and I. Figure S4c-f further show that these grains are relatively Cs-rich, most likely because the perovskite's organic cations were vaporised during ablation.

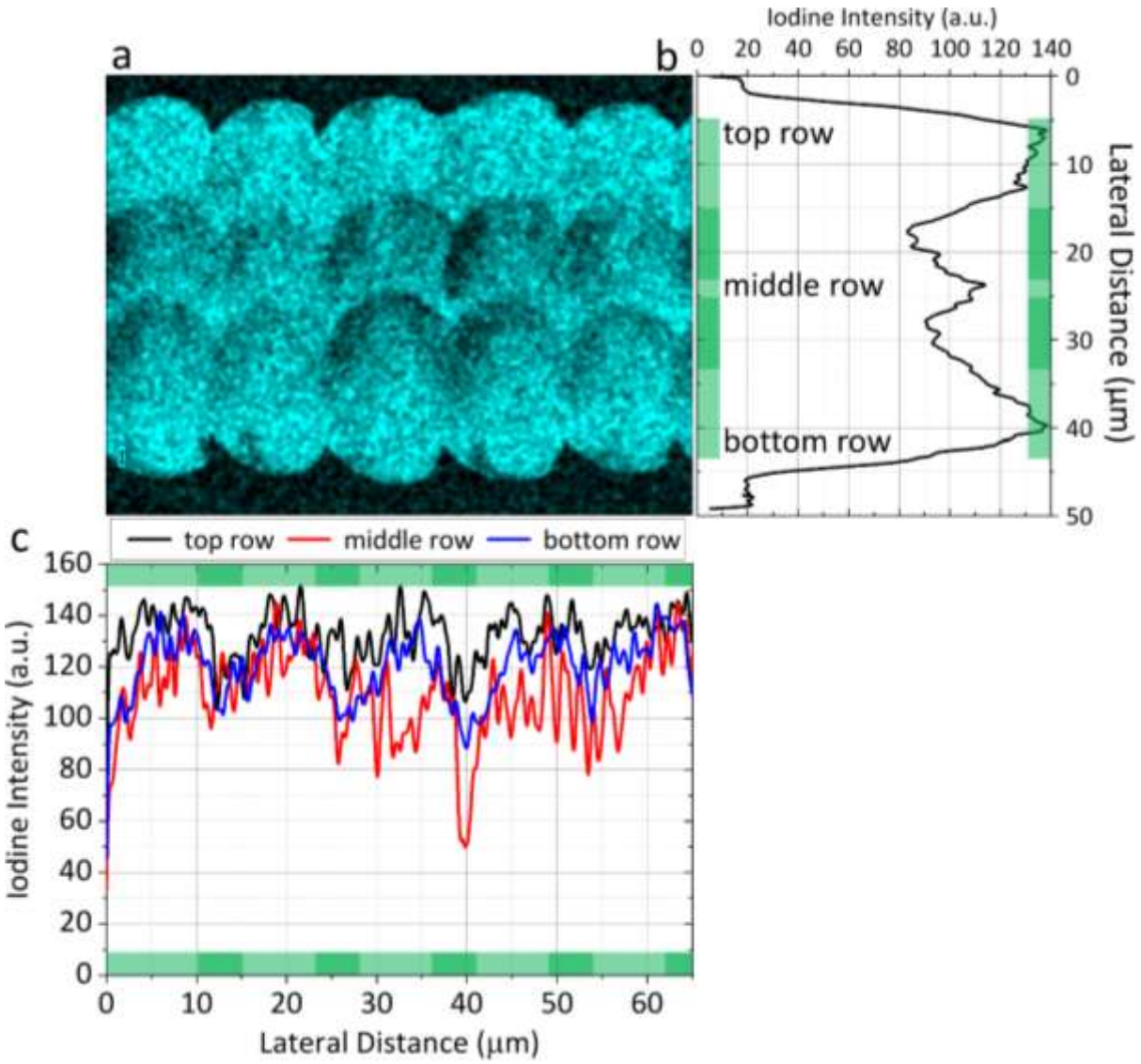

Figure S5. (a) SEM-EDX I map of sample SS. (b) Plot of horizontally averaged I intensity from (a). The green strips mark the position of the laser pulses, with darker shading indicating pulse overlaps. A section of the plot corresponding to each pulse row is marked. (c) Plot of vertically averaged I intensity for each pulse row in (a).

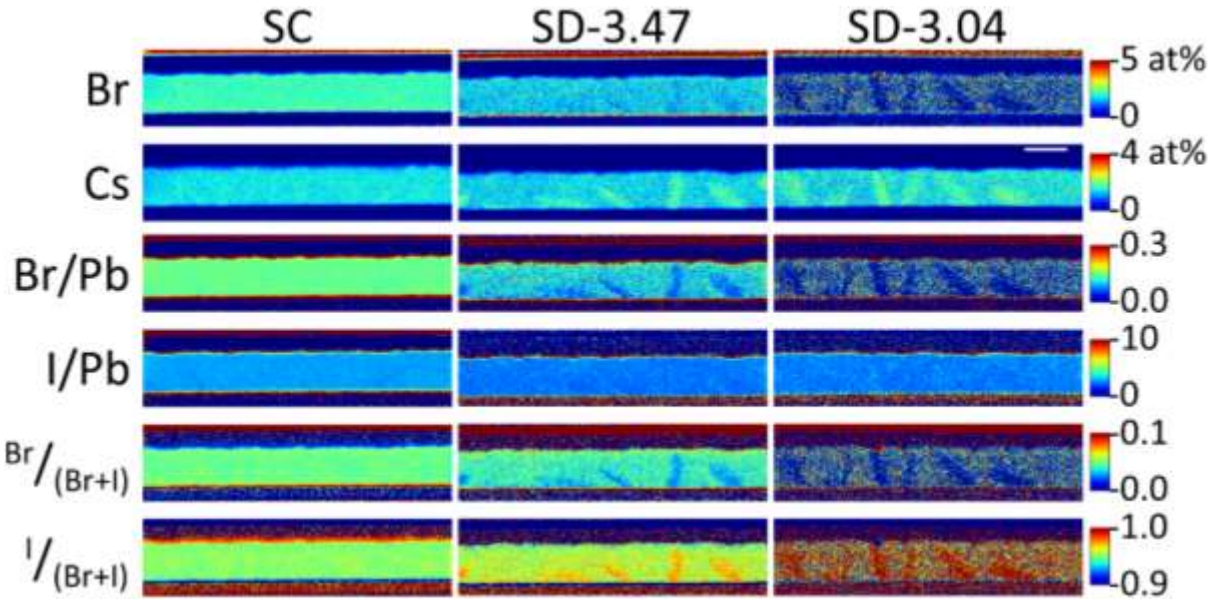

Figure S6. Additional cross-sectional STEM-EDX elemental maps for laser fluence effect comparison. The thin red strips at the perovskite - spiro-OMeTAD interface in halogen/Pb maps indicate halide migration caused by the TEM electron beam. Note that the high levels of Br in the gold layer was caused by partial EDX peak overlap between Br-K_α and the very intense Au-L_β peak there. Similarly, the higher Cs signal at the PbI_2 flakes was caused by overlap between Cs-L_α and I-L_β peaks. The scale bar is 500 nm and applies for all maps.

Supplementary Note 3

To examine the composition of the large grains which appear bright in the STEM-HAADF images, we sliced the STEM-EDX spectrum image of sample SC to isolate a grain and analysed it in HyperSpy. The dataset was decomposed with a non-negative matrix factorisation (NMF) algorithm following an established procedure, producing two significant components as shown in Figure S7.[10]

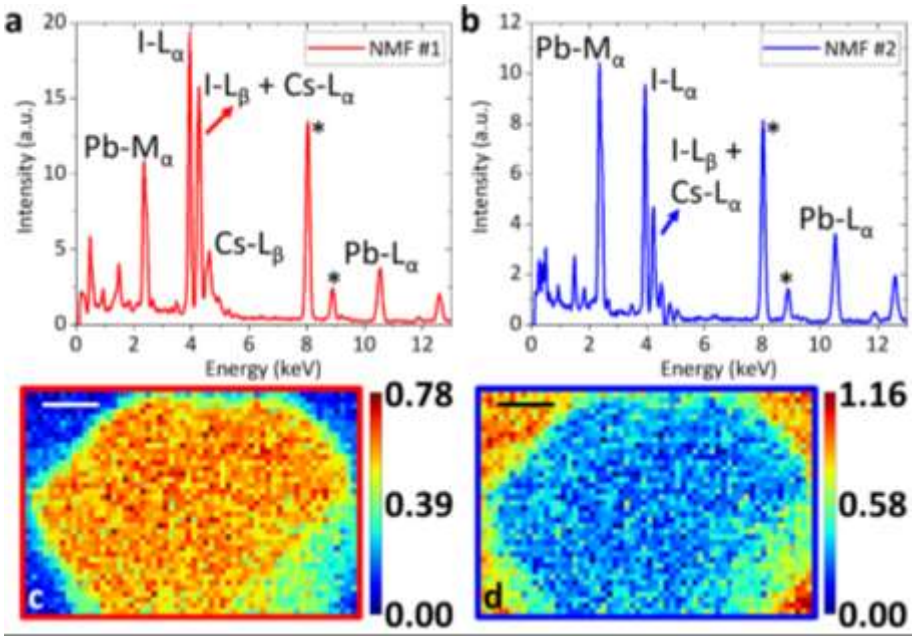

Figure S7. (a,b) Factors and (c,d) loadings of the two significant NMF components. The asterisk (*) in (a,b) mark Cu peaks from the TEM sample grid. Scale bars are 100 nm. Values represented by the colours in (c,d) are in a.u.

Based on the component loadings, we can conclude that component NMF #1 is the bright grain itself while NMF #2 is the bulk perovskite surrounding it. The two components have the same absolute intensities of Pb peaks in their factors, but the intensities of I and Cs peaks are markedly different. The I-L_α peak is more intense in NMF #1, indicating a higher concentration of I in the bright grain compared to the bulk perovskite. The Cs concentration is not as simple to determine because its L_α peak overlaps with the I-L_β peak. However, by comparing the ratio between this overlapped peak (marked I-L_β + Cs-L_α in Figure S7a,b) and the I-L_α peak across both components, we can tell that the contribution of Cs-L_α peak is much higher in NMF #1 because the I-L_β / I-L_α intensity ratio is fixed. The high Cs content in NMF #1 is confirmed by the strong Cs-L_β peak, which is very weak in NMF #2. From this analysis, we infer that these grains are remnants of CsI which only partially reacted with the other precursors to form a perovskite with a distinct stoichiometry from the bulk one.

Supplementary Note 4

We conducted threshold analysis on the cross-sectional HAADF images of samples SC and SD-3.47 to measure the volume fraction occupied by PbI_2 in the perovskite layer. We found that this fraction increased significantly from 6.65% in sample SC to 15.84% in sample SD-3.47 (Figure S8,S9). The steps in this analysis are as follows:

1. Crop the HAADF images such that only the perovskite layer remains. Further, we cropped out sections of the image with the large bright grains such as that shown in Supplementary Note 1 to remove their effect on the thresholding.
2. Extract a histogram of brightness values. Remove the lowest-intensity peak which belonged to spiro-OMeTAD pixels. Fit the remaining two peaks (perovskite, red and PbI_2, green) with Gaussian fitting.
3. Run an initial thresholding to isolate the remaining spiro-OMeTAD pixels. The threshold limits used here are from 0 to X. The value of X can be easily determined by eye as the intensity of spiro-OMeTAD pixels is far below other pixels.
4. Run the final thresholding to separate bulk perovskite and PbI_2. The threshold limits here are X to Y for perovskite and Y to 65535 for PbI_2, with Y being the crossover point of the two fitted peaks.
5. From both thresholding rounds, note the percentage of pixels occupied by spiro-OMeTAD, perovskite, and PbI_2.

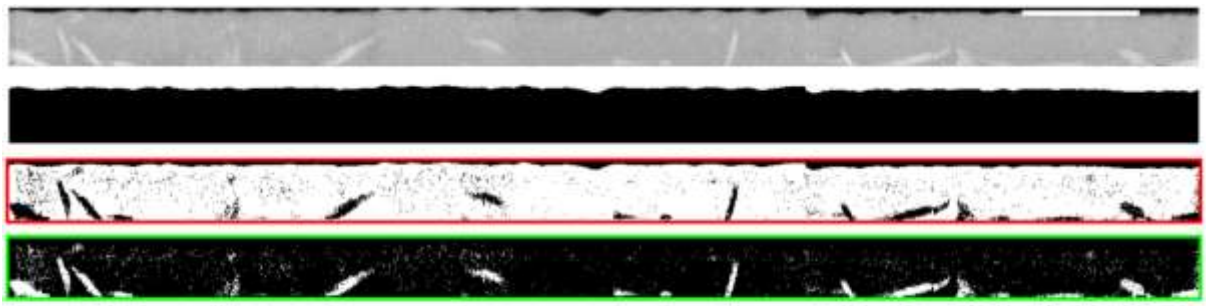

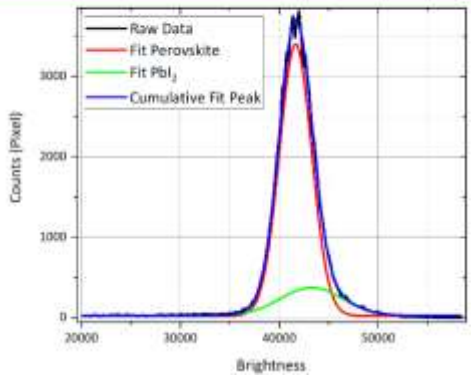

X	26780
Y	45288
Spiro-OMeTAD	7.06%
Perovskite	86.76%
PbI_2	6.18%
PbI_2 / (PbI_2 + perovskite)	6.65%

Figure S8. Threshold analysis results for sample SC. From top to bottom, the images are cropped HAADF image, initial thresholding result (white = spiro-OMeTAD, black = perovskite and PbI_2), final thresholding result (white = perovskite, black = spiro-OMeTAD and PbI_2), and PbI_2 grains (white = PbI_2, black = perovskite and spiro-OMeTAD). At the bottom are the brightness histogram with fitted peaks and analysis results in a table. The scale bar is 1 μm and applies for all images.

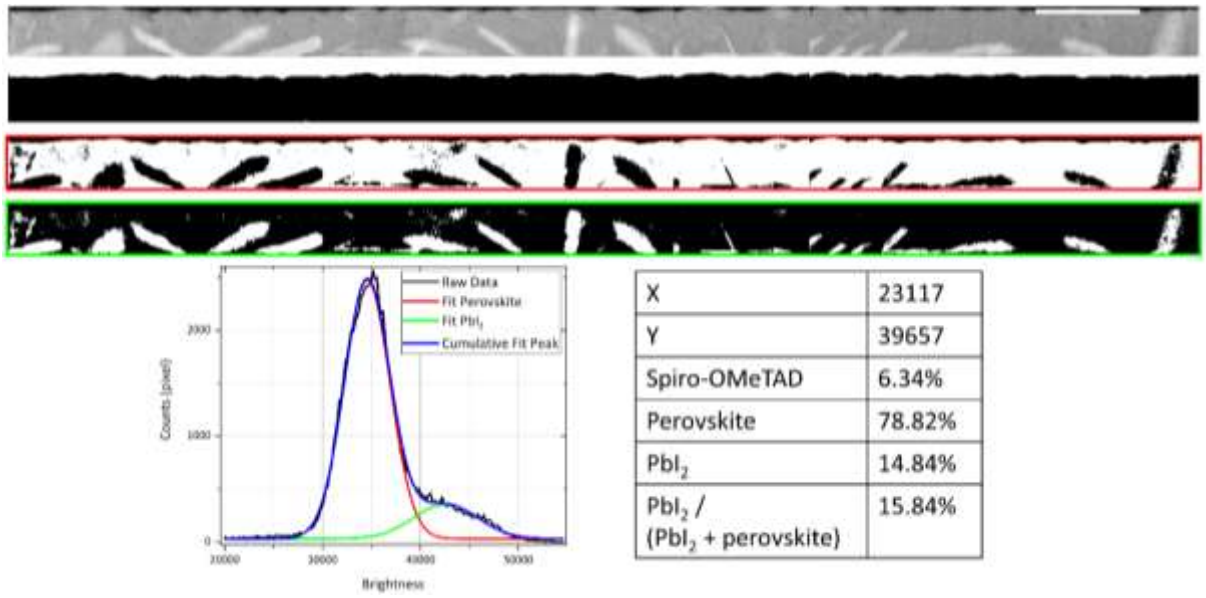

X	23117
Y	39657
Spiro-OMeTAD	6.34%
Perovskite	78.82%
PbI_2	14.84%
PbI_2 / (PbI_2 + perovskite)	15.84%

Figure S9. Threshold analysis results for sample SD-3.47. From top to bottom, the images are cropped HAADF image, initial thresholding result (white = spiro-OMeTAD, black = perovskite and PbI_2), final thresholding result (white = perovskite, black = spiro-OMeTAD and PbI_2), and PbI_2 grains (white = PbI_2, black = perovskite and spiro-OMeTAD). At the bottom are the brightness histogram with fitted peaks and analysis results in a table. The scale bar is 1 μm and applies for all images.

Supplementary Note 5

We performed a finite element analysis-based modelling of the thermal flow inside a laser-scribed PSC sample just after a laser pulse ends. The objective is not to model the material ablation process itself, whose high complexity is increased even further by the multi-layered nature of our devices. Rather, the goal here is to qualitatively map the heat flux of the residual thermal energy to see where it flows in the device stack. We used the steady-state heat transfer module in QuickField software to capture a snapshot of the heat flow.

First, we calculated two essential parameters to delineate the heat sources. Both values calculated below are for the gold back contact as the first layer hit by the laser pulse. Relevant physical properties of the gold layer are summarised in Table S1 and laser parameters in Table S2.

Physical Property	**Value**
Thickness (t)	80 nm
Absorption Coefficient at 355 nm (α)	67.623 μm^{-1}[11]
Thermal Diffusivity (D)	1.2 $cm^2 s^{-1}$[12]

Table S1. Properties of the gold layer used in modelling the heat source fronts.

Laser Parameter	**Value**
Pulse Spot Diameter (d)	18 μm
Pulse Duration (τ)	10 ps

Table S2. Laser pulse parameters used in modelling the heat source fronts.

Optical Penetration Depth

$$l_a = {}^1/_\alpha$$

l_α was calculated to be 15 nm. As l_α is significantly less than t, all laser photons were absorbed in the gold layer.

Heat Diffusion Length

$$l_T = 2\sqrt{D\tau}$$

l_T was calculated to be 70 nm. l_T gives the average distance over which heat propagates in time τ. In the context of laser ablation and with τ = pulse duration, l_T provides a measure of thermal energy spread in the target material during laser irradiation due to thermal conduction.[13,14] This residual energy will then propagate further into the bulk material, which is what we are modelling here.

With these two characteristic distances, we can now describe the model's heat sources as illustrated (not to scale) in Figure S10 below. The nature of these heat source fronts is subject to the following approximations and simplifications:

1. The shape of the heat source fronts should have followed the laser beam's Gaussian nature. However, both l_α and l_T are very small compared to the pulse spot radius (9 μm), so both the horizontal and vertical heat source fronts can be approximated as straight lines.
2. As $l_\alpha + l_T > t$, the deepest 5 nm of the middle heat source front should have been located in the spiro-OMeTAD layer. However, spiro-OMeTAD's thermal diffusivity is expected to be much lower than gold. Therefore, the value of l_T approaches zero in the spiro-OMeTAD layer and the heat source front was placed at the gold – spiro-OMeTAD interface instead.
3. The heat source fronts were estimated to have a temperature of 700 K (427°C). It is not possible to accurately approximate the actual temperature just as the laser pulse ends due to the high complexity of laser-material interactions. Schultz and colleagues previously estimated that an ns-pulse laser with fluence < 1.5 Jcm^{-2} can induce a local temperature of several hundred K above room temperature.[15] As our work uses a ps-pulse laser with less residual heat, we believe that the maximum temperature rise here would be in the low end of Schultz et al's approximation. Regardless, high accuracy of this parameter is not essential as this model is not intended to provide quantitative information. We note that decomposition of perovskite into PbI_2 has been observed at temperatures as low as 85°C, so PbI_2 growth discussed in the main text is not incompatible with the temperature estimation used here.[16]

Figure S10. Illustration of the heat source fronts (red lines) used to model thermal energy flow after a laser pulse.

Other than the heat source fronts, other important details of the model are:

1. The side edges of all layers and the bottom edge of the glass substrate layer are modelled as heat sinks with a temperature of 298 K (25°C).
2. Heat loss at the gold layer's top surface (gold-N_2 interface) is modelled as natural convection of heat in a nitrogen atmosphere. The convection coefficient was calculated in QuickField to be 126 $Wm^{-2}K^{-1}$.[17]
3. Thermal conductivities and thicknesses of the material layers are described in Table S3. Thermal conductivity values were measured at temperatures lower than the relevant range for this model. Regardless, they are used here due to lack of experimental data at the appropriate temperatures.

4. PbI_2 needles occupied ~6.7% of the perovskite layer's volume, as measured in Supplementary Note 4.

Layer	Thermal Conductivity ($Wm^{-1}K^{-1}$)	Modelled Thickness (nm)
Gold	310[12]	80
Spiro-OMeTAD	0.1 (estimated)	250
Perovskite	0.3[18–21]	500
PbI_2	2.7[22]	N.A.
SnO_2	40[23]	20
ITO	5.6[24]	150
Glass	0.8[25]	1000

Table S3. Thermal conductivity and thickness of each device layer in the thermal flow model.

The result of our modelling shows that heat flows through the gold layer much faster than in other layers as expected from its high thermal conductivity (Figure S11). As the thermal energy propagates laterally through gold, some of it travels downwards. Within the perovskite layer, there is a funnelling effect as the heat passes through PbI_2 needles about 8-9x faster than through the perovskite grains (Figure S12). This model thus shows that during laser scribing, a significant portion of the residual thermal energy which flows through the perovskite layer will travel through PbI_2 if it is present. This conclusion validates our proposed thermal flow mechanism.

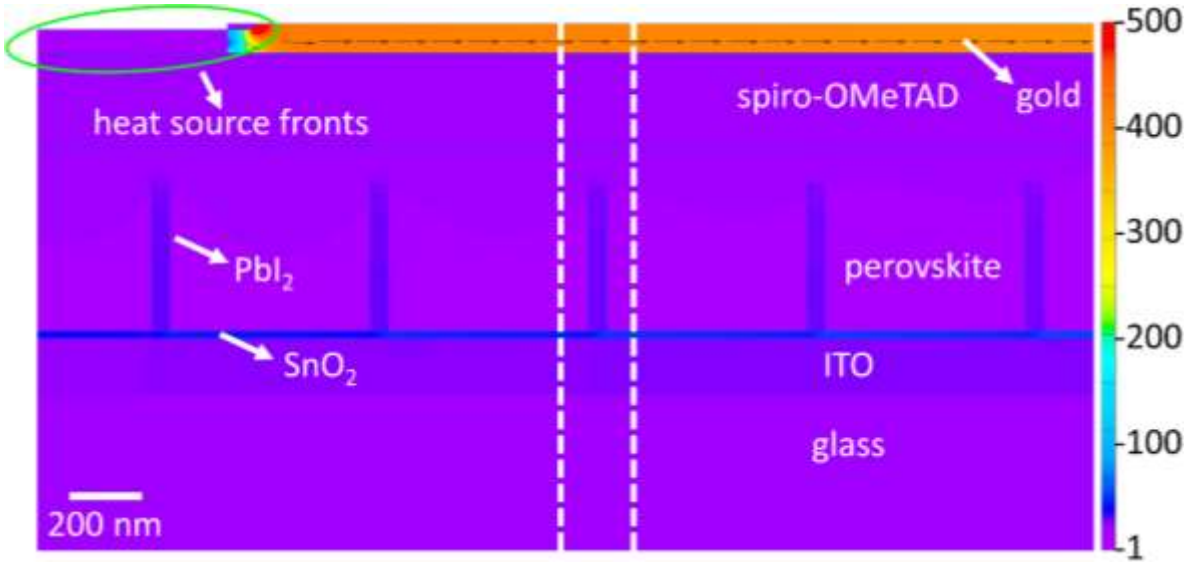

Figure S11. Heat flux map produced by the thermal flow model. The right-side half of the heat source fronts shown in Figure S10 is marked by the green oval. Arrows indicate direction and magnitude of the heat flux (the flux in layers other than gold is so small in comparison that the arrows are not visible, see Figure S12). The white dashed lines delineate the position of the lamellae cut parallel to the P3 lines, ~900 nm away from the scribe line edge. Numbers on the colour bar are in 10^7 Wm^{-2}.

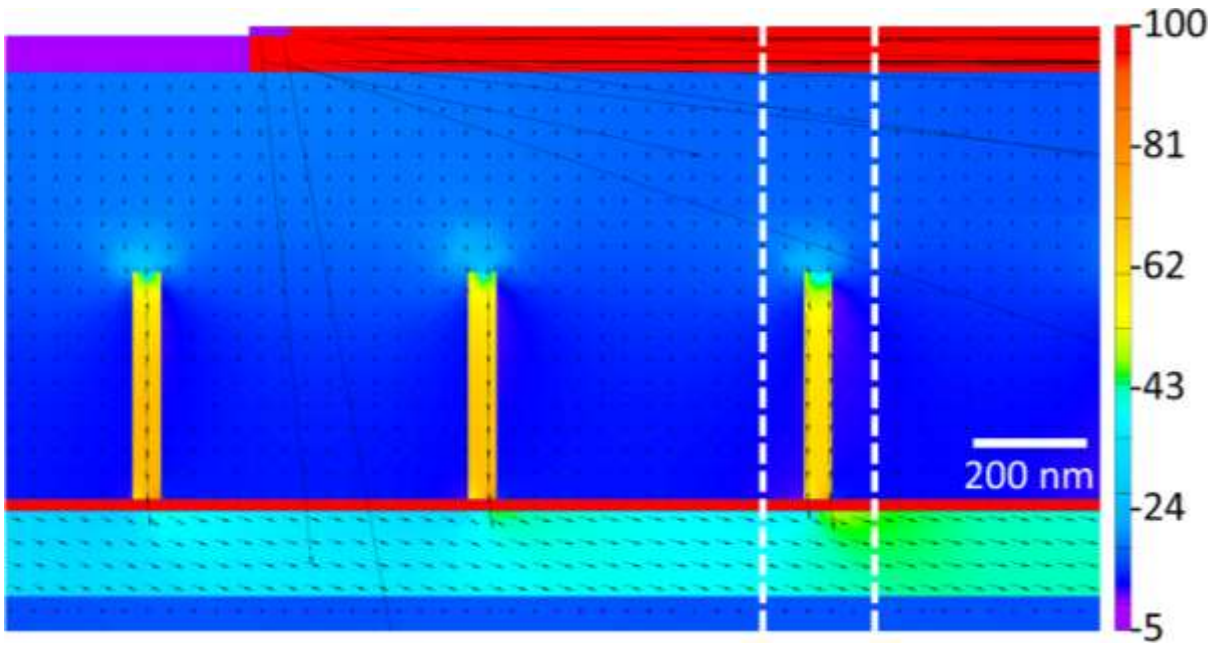

Figure S12. Heat flux map produced by the thermal flow model. Arrows indicate direction and magnitude of the heat flux. The white dashed lines delineate the position of the lamellae cut parallel to the P3 lines, ~900 nm away from the scribe line edge. Numbers on the colour bar are in 10^6 Wm^{-2}

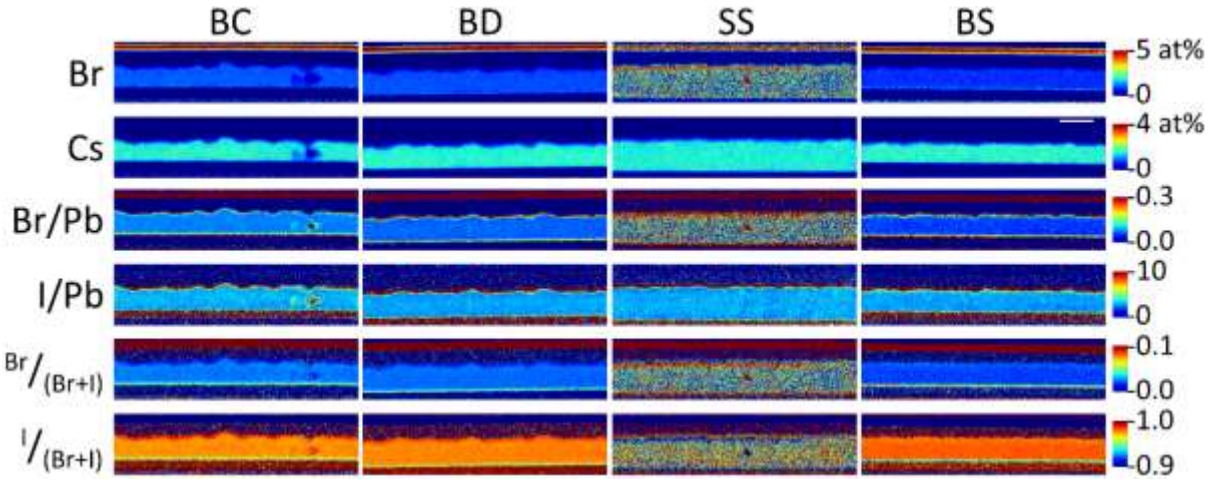

Figure S13. Additional cross-sectional STEM-EDX elemental maps for samples BC, BD, SS, and BS. The thin red strips at the perovskite - spiro-OMeTAD interface in halogen/Pb maps indicate halide migration caused by the TEM electron beam. Note that the high levels of Br in the gold layer was caused by partial EDX peak overlap between Br-K_α and the very intense Au-L_β peak there. Similarly, the higher Cs signal at the PbI_2 flakes was caused by overlap between Cs-L_α and I-L_β peaks. The scale bar is 500 nm and applies for all maps.

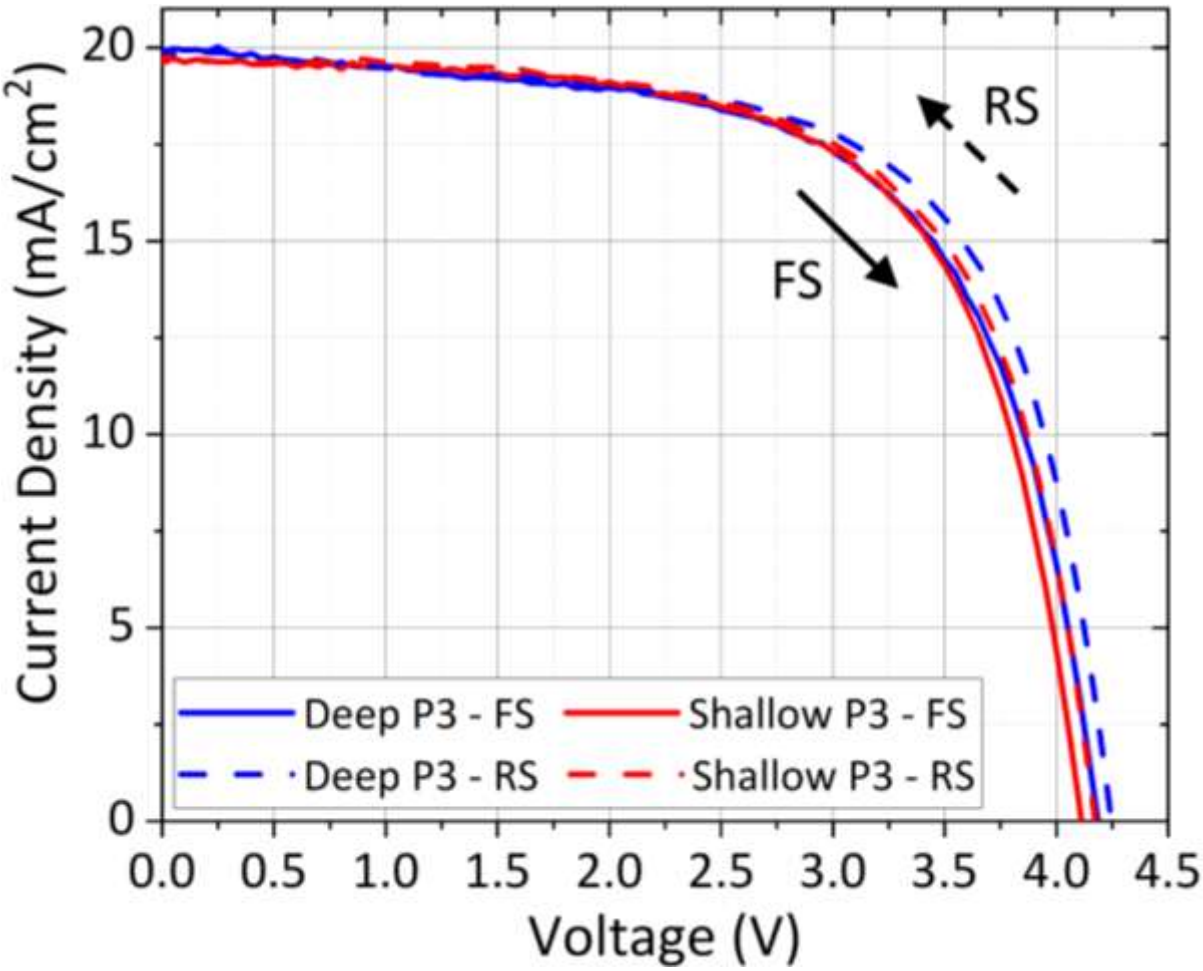

Figure S14. J-V curves of blade-coated devices using deep or shallow P3 lines. The solid lines are forward scan (FS) sweep, from -0.5 V to +4.5 V. The dashed lines are reverse scan (RS) sweep, from +4.5 V to -0.5 V. The scan rate was 4 V/s with a measurement delay of 10 ms.

Sample	V_{OC} (V)	J_{SC} ($mAcm^{-2}$)	FF (%)	PCE (%)	MPPT PCE (%)
Deep P3 – FS	4.20	19.9	63.1	13.19	13.1
Deep P3 – RS	4.25	19.9	65.5	13.85	
Shallow P3 – FS	4.10	19.6	65.8	13.20	13.1
Shallow P3 – RS	4.15	19.6	65.9	13.42	

Table S4. Photovoltaic parameters of blade-coated devices using deep or shallow P3 lines. The MPPT PCE was obtained at the 5-minute mark.

Current-voltage measurements

Perovskite modules used for the JV measurement consisted of four serially interconnected monolithic cells with an aperture area of 4 cm^2 and geometrical fill factor of 94%. Modules were measured in an N_2-filled glovebox and illuminated using a class AAA solar simulator (Abet Sun 3000) with AM1.5G spectrum at 1 sun intensity. The solar simulator lamp was calibrated with a Fraunhofer ISE certified silicon reference cell with KG3 filter. J-V sweeps were performed using hysteresis scan from open circuit to short circuit and back to open circuit in voltage range from -0.5 to 4.5 V, voltage step of 0.05 V and measurement delay of 10 ms. The J-V scan rate is 4 V/s per module or 1 V/s per cell in a module.

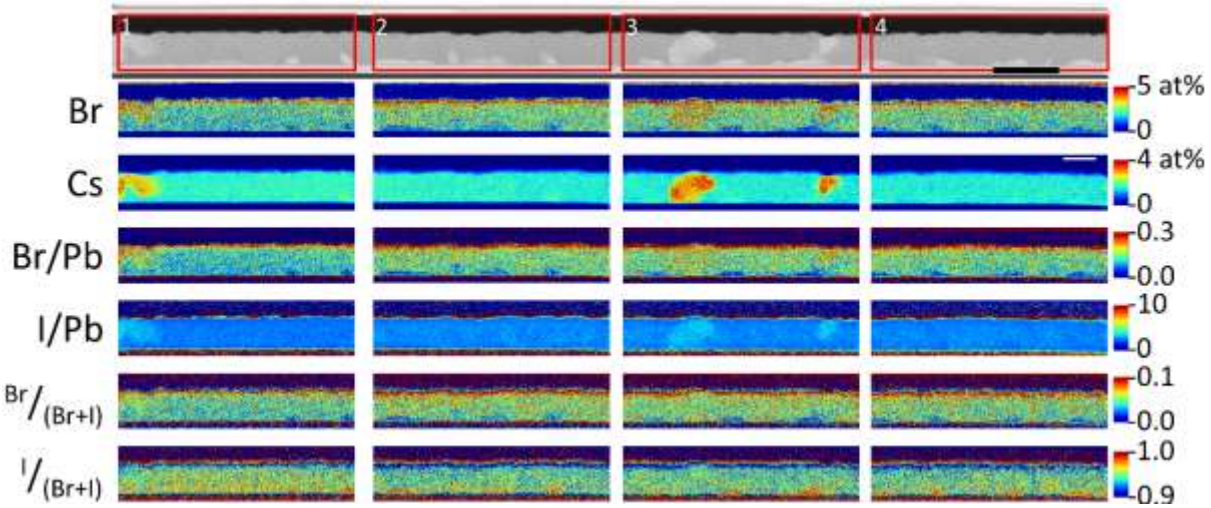

Figure S15. Cross-sectional STEM-HAADF image and additional STEM-EDX elemental maps of a perpendicular-to-scribe lamella taken from sample SD-3.04. Each red box represents a STEM-EDX scan area corresponding to the maps below it. The scale bar is 1 μm for the STEM-HAADF image and 500 nm for the elemental maps. The thin red strips at the perovskite - spiro-OMeTAD interface in halogen/Pb maps indicate halide migration caused by the TEM electron beam.

References

1 J. Bonse, S. Hohm, S. V. Kirner, A. Rosenfeld and J. Kruger, *IEEE J. Sel. Top. Quantum Electron.*, , DOI:10.1109/JSTQE.2016.2614183.

2 K. Sugioka and Y. Cheng, *Light Sci. Appl.*, 2014, **3**, e149–e149.

3 M. Huang, F. Zhao, Y. Cheng, N. Xu and Z. Xu, *ACS Nano*, 2009, **3**, 4062–4070.

4 J. Bonse, A. Rosenfeld and J. Krüger, *J. Appl. Phys.*, 2009, **106**, 104910.

5 G. Miyaji and K. Miyazaki, *Opt. Express*, 2008, **16**, 16265.

6 F. Garrelie, J.-P. Colombier, F. Pigeon, S. Tonchev, N. Faure, M. Bounhalli, S. Reynaud and O. Parriaux, *Opt. Express*, 2011, **19**, 9035.

7 Y. Katsumata, T. Morita, Y. Morimoto, T. Shintani and T. Saiki, *Appl. Phys. Lett.*, 2014, **105**, 031907.

8 D. Puerto, M. Garcia-Lechuga, J. Hernandez-Rueda, A. Garcia-Leis, S. Sanchez-Cortes, J. Solis and J. Siegel, *Nanotechnology*, 2016, **27**, 265602.

9 J. I. Goldstein, D. E. Newbury, J. R. Michael, N. W. M. Ritchie, J. H. J. Scott and D. C. Joy, *Scanning Electron Microscopy and X-Ray Microanalysis*, Springer New York, New York, NY, 2018.

10 S. Cacovich, F. Matteocci, M. Abdi-Jalebi, S. D. Stranks, A. Di Carlo, C. Ducati and G. Divitini, *ACS Appl. Energy Mater.*, 2018, **1**, 7174–7181.

11 D. I. Yakubovsky, A. V. Arsenin, Y. V. Stebunov, D. Y. Fedyanin and V. S. Volkov, *Opt. Express*, 2017, **25**, 25574.

12 D. Bäuerle, *Laser Processing and Chemistry*, Springer Berlin Heidelberg, Berlin, Heidelberg, 2011.

13 M. S. Brown and C. B. Arnold, 2010, pp. 91–120.

14 X. Liu, D. Du and G. Mourou, *IEEE J. Quantum Electron.*, 1997, **33**, 1706–1716.

15 C. Schultz, F. Schneider, A. Neubauer, A. Bartelt, M. Jost, B. Rech, R. Schlatmann, S. Albrecht and B. Stegemann, *IEEE J. Photovoltaics*, 2018, **8**, 1244–1251.

16 B. Conings, J. Drijkoningen, N. Gauquelin, A. Babayigit, J. D'Haen, L. D'Olieslaeger, A. Ethirajan, J. Verbeeck, J. Manca, E. Mosconi, F. De Angelis and H. G. Boyen, *Adv. Energy Mater.*, 2015, **5**, 1–8.

17 Tera Analysis Ltd., Natural convection coefficient calculator, https://quickfield.com/natural_convection.htm, (accessed 18 June 2019).

18 A. Pisoni, J. Jaćimović, O. S. Barišić, M. Spina, R. Gaál, L. Forró and E. Horváth, *J. Phys. Chem. Lett.*, 2014, **5**, 2488–2492.

19 A. Kovalsky, L. Wang, G. T. Marek, C. Burda and J. S. Dyck, *J. Phys. Chem. C*, 2017, **121**, 3228–3233.

20 Z. Guo, S. J. Yoon, J. S. Manser, P. V. Kamat and T. Luo, *J. Phys. Chem. C*, 2016, **120**, 6394–6401.

21 M. Wang and S. Lin, *Adv. Funct. Mater.*, 2016, **26**, 5297–5306.

22 T. S. Silva, A. S. Alves, I. Pepe, H. Tsuzuki, O. Nakamura, M. M. F. d'Aguiar Neto, A. F. da Silva, N. Veissid and C. Y. An, *J. Appl. Phys.*, 1998, **83**, 6193–6195.

23 L. Gmelin, *Handbuch der Anorganischen Chemie*, 8th edn., 1967.

24 T. Ashida, A. Miyamura, N. Oka, Y. Sato, T. Yagi, N. Taketoshi, T. Baba and Y. Shigesato, *J. Appl. Phys.*, 2009, **105**, 073709.

25 H. D. Young and R. A. Freedman, *University Physics with Modern Physics*, Pearson, 14th edn., 2014.